The allosteric mechanism of substrate-specific transport in SLC6 is mediated by a volumetric sensor

Michael V. LeVine[a,b,1,2], Daniel S. Terry[a,1], George Khelashvili[a,b], Zarek S. Siegel[a,b], Matthias Quick[c,d], Jonathan A. Javitch[c,d,e], Scott C. Blanchard[a], and Harel Weinstein[a,b,2]

[a]Department of Physiology and Biophysics, Weill Cornell Medicine, New York, NY 10065; [b]HRH Prince Alwaleed Bin Talal Bin Abdulaziz Alsaud Institute for Computational Biomedicine, Weill Cornell Medicine, New York, NY 10021; [c]Department of Psychiatry, Vagelos College of Physicians and Surgeons, Columbia University, New York, NY 10032; [d]Division of Molecular Therapeutics, New York State Psychiatric Institute, New York, NY 10032; and [e]Department of Pharmacology, Vagelos College of Physicians and Surgeons, Columbia University, New York, NY 10032

Edited by Susan G. Amara, National Institutes of Health, Bethesda, MD, and approved June 24, 2019 (received for review February 20, 2019)

Neurotransmitter:sodium symporters (NSSs) in the SLC6 family terminate neurotransmission by coupling the thermodynamically favorable transport of ions to the thermodynamically unfavorable transport of neurotransmitter back into presynaptic neurons. Results from many structural, functional, and computational studies on LeuT, a bacterial NSS homolog, have provided critical insight into the mechanism of sodium-coupled transport, but the mechanism underlying substrate-specific transport rates is still not understood. We present a combination of molecular dynamics simulations, single-molecule fluorescence resonance energy transfer (smFRET) imaging, and measurements of Na^+ binding and substrate transport that reveals an allosteric substrate specificity mechanism. In this mechanism, residues F259 and I359 in the substrate binding pocket couple the binding of substrate to Na^+ release from the Na2 site by allosterically modulating the stability of a partially open, inward-facing state. We propose a model for transport selectivity in which residues F259 and I359 act as a volumetric sensor that inhibits the transport of bulky amino acids.

allostery | transporters | neurotransmitters

Neurotransmitter:sodium symporters (NSSs) in the SLC6 family are secondary active transport proteins that regulate the extent and duration of neurotransmission events by reimporting neurotransmitter molecules following their release into the postsynaptic space (1). The critical function of these transporters in regulating neurotransmission is highlighted by their specific targeting by small molecules, including clinically important antidepressants and psychostimulant drugs of abuse (2, 3). The transport mechanism of NSS family members is thought to involve conformational changes that control accessibility of the transporter to the intracellular and extracellular milieu of the cell in alternating fashion (4), where the net transport of substrates against their concentration gradient is powered by transmembrane electrochemical Na^+ gradients.

While the thermodynamic features of secondary active transport are well understood, intense study is currently focused on the identification of the specific sequence of substrate binding and release events, as well as the series of conformational changes that are coupled to, and facilitate, these processes (5–17). X-ray crystallographic studies have provided insight into the NSS molecular architecture, beginning with crystal structures of the Na^+-coupled prokaryotic amino acid transporter LeuT (18, 19), which allowed for existing mechanistic models to be put into a structural context (20). Single-molecule fluorescence resonance energy transfer (smFRET) studies have illuminated the dynamic sampling of functionally important intermediate states visited by the transporter during the transport cycle (21–23). Computational studies employing molecular dynamics (MD) simulation have identified key elements of the complex allosteric mechanism by which conformational changes in the transporter are coupled to the binding and release of ions and substrates (1, 9, 17, 24–30).

Our previously described smFRET experiments (21–23) reported on the displacement of the N terminus from the intracellular gate at the center of the transmembrane helical bundle in LeuT. Before disengagement, residues within the N terminus contribute to a critical network of interactions, including a salt bridge and a number of hydrogen bonds that maintain NSS proteins in an inward-closed conformation in which the substrate is occluded from the intracellular solvent. The smFRET data initially revealed 2 states: a high-FRET state that corresponded to an inward-closed conformation (denoted IC) and a low-FRET state that corresponded to an inward-open conformation (denoted IO) in which the N terminus has dissociated from the intracellular gate such that the substrate can become exposed to the intracellular solvent. These studies (21–23), and later experiments utilizing electron pair resonance (31) and cysteine accessibility (29), probed the modulation of the IO/IC exchange process in relation to substrate occupancy in the primary substrate (S1) binding site as well as a secondary substrate (S2) binding site identified as having allosteric impacts on the transport mechanism (9, 32, 33).

Leveraging technical advances in smFRET technologies, including scientific complementary metal–oxide–semiconductor (sCMOS) imaging (34) and self-healing fluorophores (35, 36), we were recently able to identify an additional intermediate-FRET state in LeuT that was rapidly and specifically sampled in the presence of Na^+ and the rapidly transported cognate

Significance

The combination of molecular dynamics simulation, single-molecule imaging, and functional assays described here reveals a mechanism of substrate selectivity in the SLC6 family of neurotransmitter transporters. We show that the rotameric state of a volumetric sensor in the substrate binding site is allosterically coupled to conformational changes necessary for transport, and as a consequence, upon binding large substrates, the transporter becomes stabilized in an inactive, nontransporting state upon binding larger substrates. This mechanistic insight suggests the possibility that medically relevant SLC6 transporters may be targeted by inhibitors that specifically modulate this sensor.

Author contributions: M.V.L., D.S.T., G.K., M.Q., J.A.J., S.C.B., and H.W. designed research; M.V.L., D.S.T., G.K., Z.S.S., and M.Q. performed research; M.V.L., D.S.T., G.K., Z.S.S., M.Q., J.A.J., S.C.B., and H.W. analyzed data; and M.V.L., D.S.T., G.K., Z.S.S., M.Q., J.A.J., S.C.B., and H.W. wrote the paper.

Conflict of interest statement: S.C.B. has an equity interest in Lumidyne Technologies.

This article is a PNAS Direct Submission.

[1]M.V.L. and D.S.T. contributed equally to this work.

[2]To whom correspondence may be addressed. Email: mil2037@med.cornell.edu or haw2002@med.cornell.edu.

This article contains supporting information online at www.pnas.org/lookup/suppl/doi:10.1073/pnas.1903020116/-/DCSupplemental.

Published online July 19, 2019.

substrate Ala, which we found to be consistent with a partially inward-open conformation (23) (denoted here as IO2). Notably, the IO2 state was not appreciably occupied in the presence of the slowly transported substrate Leu, or when Na^+ was replaced with Li^+ during Ala binding. We also found that the Ala-stabilized IO2 state was selectively disfavored by high Na^+ concentrations, consistent with it corresponding to a conformation in which only 1 Na^+ binding site is occupied. These findings are globally consistent with computational (9, 17, 37) and experimental (9) evidence suggesting that the Na^+ release from the Na2 site is the obligatory first step of the substrate transport mechanism.

As Ala exhibits a substantially greater maximum velocity of transport (V_{max}) than Leu, we hypothesized that substrate-specific stabilization of the IO2 state may trigger the release of Na^+ from the Na2 site to allow transport to proceed. By extension, substrate-specific stabilization of the IC state may inhibit Na^+ release to such an extent that exit from this state becomes a rate-determining step with regard to the overall transport process. This model is consistent with recent analyses performed for the human dopamine transporter, which revealed an allosteric coupling between Na^+ release from the Na2 site and inward opening (16, 17, 37).

Despite a multitude of advances toward quantifying substrate-specific allosteric modulation of intracellular gating and Na^+ release by substrates, the molecular basis of the transport mechanism has yet to be fully delineated. To shed light on the allosteric control mechanism underpinning NSS transport, we (17, 24, 38, 39) and others (40–43), have developed computational methods and theoretical models, including N-body information theory (NbIT) analyses (24, 38) and the thermodynamic coupling function (TCF) theory of allostery (17, 39). Previously, we applied NbIT analysis to MD simulation of LeuT bound to Na^+ and Leu in an occluded state (24) to identify significant information transmission between the S1 site and the intracellular gate. In this study, information transmission was evidenced via the S1 substrate's direct interaction with the conserved F259 residue in transmembrane helix (TM) 6b, and to a lesser extent with residue I359 in TM8. Interestingly, a comparative analysis of LeuT crystal structures bound to substrates that exhibit distinct transport rates (including Gly, Ala, Leu, Met, L-4-fluorophenylalanine [L-4-FP], and Trp) revealed characteristic differences in the mode of substrate interactions with residue F259 (19). Specifically, Trp (like L-4-FP), which acts as an inhibitor of transport, was observed to make strong ring–ring contacts with F259. By contrast, Met and Leu, which are slowly transported substrates, were observed to exhibit weaker hydrophobic interactions with F259, whereas Ala, which is efficiently transported, makes no contact with F259. A similar (albeit smaller) difference in the mode of interaction of I359 with the substrates was also apparent. These investigations, combined with the substrate-specific allosteric modulation observed for Leu and Ala in our previous smFRET experiments (22, 23), suggest the existence of a relationship between the extent of S1 substrate interactions with F259 and transport efficacy.

We therefore hypothesized that substrates that interact strongly with F259 stabilize the IC state and quench the gating dynamics required for transport, whereas substrates that interact weakly with F259 stabilize the IO2 state, trigger release of Na^+ from the Na2 site, and facilitate transport. To examine this hypothesis, we combined microsecond-scale MD simulations, hybrid quantum mechanics/molecular mechanics (QM/MM) calculations, and transport and smFRET experiments in the analysis of LeuT in complex with the substrates Gly, Ala, Val, and Leu. Our results suggest a mechanism in which F259, assisted by I359, acts as a volumetric sensor that allosterically couples the chemical identity of the substrate to different extents of inward closing in a manner that substrate-specifically modulates the intracellular release of Na^+ from the Na2 site.

Results

Differential Modulation of F259 and I359 Rotamer Dynamics by Substrates. LeuT can bind and transport a number of neutral, hydrophobic amino acid substrates (19) that are proposed to share a mechanism of transport involving allosteric interactions in the S1 and S2 sites (9, 44). Whereas the transport and binding kinetics vary significantly among these different substrates (including Gly, Ala, Val, and Leu), the crystal structures of LeuT in complex with each of these ligands displayed only subtle changes (19). Specifically, the Ala- and Gly-bound structures display only a 30° rotation of the F259 χ_2 angle and a ∼15° rotation of the I359 χ_1 angle compared with the Leu-bound structure. Because we had previously identified both of these residues as significant mediators of information transmission between the S1 binding site and the intracellular gate in the Leu-bound state (24), we hypothesized that there exists a relation between substrate-specific differences in experimentally measured V_{max} and the modulation of the conformational dynamics of F259 and I359. To investigate the possibility that subtle rotations of F259 and I359 identified in the X-ray structure reflect larger differences in conformational flexibility or heterogeneity under physiological conditions, we investigated a panel of protein–substrate complexes that allowed for a systematic evaluation of how the graded reduction of the interaction between substrate and the F259 and I359 side chains may affect the conformational dynamics of these 2 residues.

Microsecond-scale, all-atom MD simulations and rotamer scan QM/MM calculations were carried out for LeuT in complex with Gly, Ala, Val, and Leu (*Methods*). The results showed that both F259 and I359 sample multiple conformational states at room temperature, and do so in a substrate-dependent manner. In particular, we found that when LeuT is bound to Ala and Gly, which have relatively small side chains, F259 freely rotates between 4 χ_2 angle states (Fig. 1 *A* and *B* and *SI Appendix*, Figs. S1, S2, and S7). The χ_2 angle describes the rotation of the phenyl ring relative to the Cα–Cβ bond. Due to the symmetric nature of the phenyl ring, these 4 rotamer states are composed of 2 sets of 2 symmetric rotameric states, referred to here as "perpendicular" and "parallel." In the perpendicular state, the F259 phenyl side chain faces the substrate (Fig. 1*A*, χ_2 angles of ∼75° and ∼255°), whereas in the parallel state, the side chain turns ∼90° (χ_2 angles of approximately −5° and ∼165°) and is aligned with the axis of the substrate. The free exchange between perpendicular and parallel states observed in our simulations is consistent with the behavior of an ideal allosteric channel in the allosteric Ising model (45).

When LeuT is bound to Val, a substrate with a larger side chain, the F259 side chain is stabilized in the perpendicular state (Fig. 1*B* and *SI Appendix*, Fig. S3), as observed in the X-ray crystal structures (19), but still exhibits free rotation between the symmetric perpendicular states on the nanosecond time scale. Interestingly, the dynamics reveal that while F259 freely rotates in both directions in the presence of Gly and Ala, the ring shows a preference for clockwise motions in the presence of Val (*SI Appendix*, Fig. S7). The Leu-bound complex shows only 1 exchange between the symmetric perpendicular F259 rotamer states in the early, nonequilibrium portion of the trajectory (Fig. 1*B* and *SI Appendix*, Figs. S4 and S7).

We also observe that the I359 side chain can sample 2 χ_1 states (*SI Appendix*, Fig. S6), which are differentially modulated by the 4 substrates in a similar fashion (*SI Appendix*, Figs. S1–S4, S8, and S9). The χ_1 angle describes the rotation of the Ile side chain relative to the Cα–N bond of the backbone. When Leu or Val is bound, I359 predominantly samples a state at 240°. By contrast, in the Gly- and Ala-bound simulations I359 predominately samples a state at 120° that was not observed in the X-ray structures of these complexes. In addition, in the Gly- and Ala-bound simulations, we

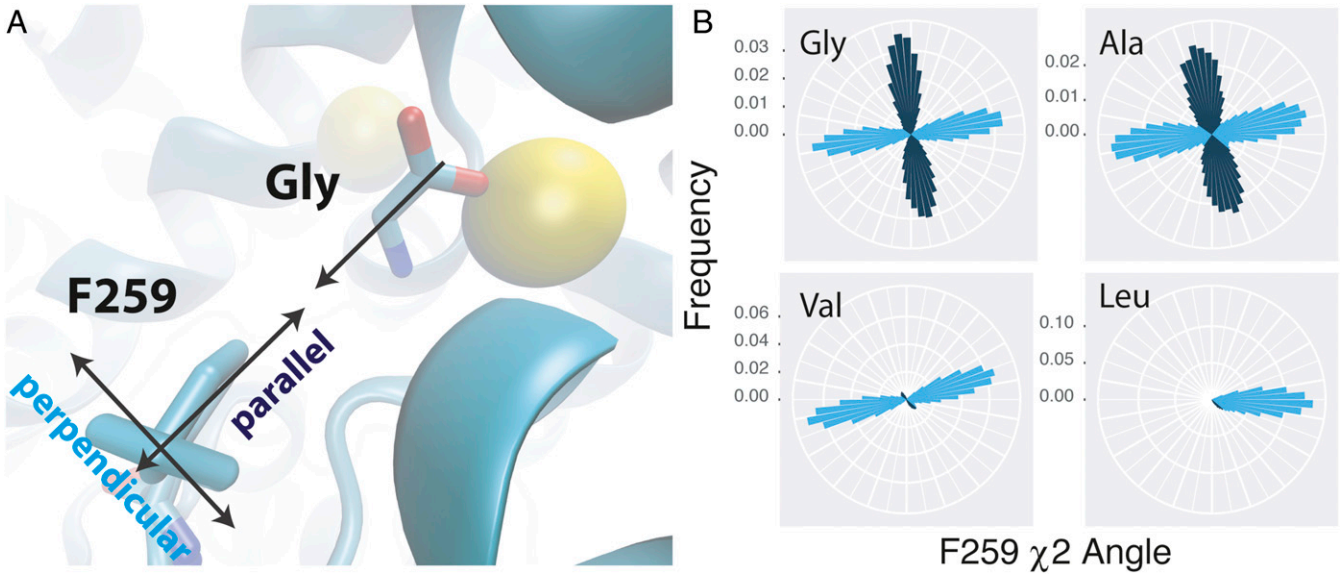

Fig. 1. Substrates differentially modulate F259 rotameric dynamics. (*A*) The 2 possible states of the F259 side chain. The substrate glycine is shown for reference, with surrounding Na1 (*Right*) and Na2 (*Left*) shown in yellow. (*B*) Rose plots showing the angular histograms of the F259 χ_2 angle sampled during the converged portion of the MD simulations, colored by angular *k*-means clustering.

observe a water molecule transiently entering the space between the S1 and Na2 sites, interacting with the Na2-binding residue S355. While occupancy was short-lived, at no point in the Leu- or Val-bound simulations did water occupy the corresponding site, which can be attributed to steric hindrance by the substrate side chains (*SI Appendix*, Fig. S10). In all systems, we also observed the formation of transient water wires that bridged the Na2 site and intracellular space (*SI Appendix*, Fig. S11). Such water wires have previously been predicted to play a role in destabilization of the Na^+ in Na2 (46), and are seen to be mediated by Y265. Notably, the Y265C mutation is known to lead to a significant loss of LeuT function (29), an effect the present findings suggest may be attributed to its role in this network.

While in the presence of Ala and Gly the F259 parallel and perpendicular states were equally probable (and 120° state for residue I359 was strongly preferred), the empirical rotamer distribution of Phe found in protein structures in the Protein Data Bank (PDB) (47) indicates that the parallel rotamer states are expected to be low probability. Thus, we hypothesized that when F259 is unhindered by the substrate side chain, the parallel state may be enthalpically unstable relative to the perpendicular state and would thus be not be observed in a low-temperature X-ray crystal structure. To investigate this possibility, we used QM/MM energy calculations to scan the angle space of both F259 and I359. In so doing, we found distinct energy wells in the F259 χ_2 potential energy landscape in our Gly- and Ala-bound QM/MM calculations (*SI Appendix*, Fig. S12). Specifically, we observed that the parallel state is ∼3 kcal higher in energy than the perpendicular state that is observed in the X-ray structure, indicating an enthalpic preference consistent with our hypothesis. In addition, the energy minimum corresponding to the parallel state is not present in the Leu-bound complex. In the Val-bound state, it is roughly 6 kcal higher in energy. Similarly, in the I359 χ_1 landscape, we find a second minimum, corresponding to the alternative conformation observed in our MD simulations (*SI Appendix*, Fig. S13), which is destabilized by roughly 3 kcal relative to the rotameric state found in the X-ray structure. As for F259, no alternative state for the I359 χ_1 angle is present in the Leu-bound complex, and the state is roughly 8 kcal higher in energy in the Val-bound complex. These calculations provide independent support for substrate-specific modulation of the rotameric state of residues F259 and I359.

Free Rotation of F259 Is Associated with Stabilization of the IO2 State. Because our previous findings implicated F259 and I359 in allosteric modulation of intracellular gate dynamics (24), we next sought to identify the relationship between substrate-dependent rotamer dynamics and the observed differences in transport rates for the various substrates. Given the observation that Ala stabilizes the inward-facing, intermediate-FRET state (IO2), whereas Leu does not (22, 23), we hypothesized that the intermediate-FRET state exhibited by LeuT's intracellular gate may be allosterically coupled to the F259 and I359 rotamer equilibriums, and in particular to transitions to the parallel state of F259. Based on this hypothesis and our MD and QM/MM results, we expect Gly (like Ala) to stabilize the IO2 state, whereas we anticipate Val (like Leu) not to do so.

To test this hypothesis, we performed smFRET imaging of the intracellular dynamics of LeuT (see *Methods* for details) in the presence of Gly, Ala, Val, and Leu and varying Na^+ concentrations. Ala and Gly both elicited Na^+-dependent stabilization of the IO2 state (Fig. 2*A*) and increased intracellular gating dynamics (Fig. 2 *B* and *C*) compared with Na^+ alone (*SI Appendix*, Fig. S14). By contrast, Val partially stabilized the inward-closed state and only slightly increased intracellular gating dynamics. Leu stabilized the inward-closed state of the intracellular gate even further and did not increase gating dynamics compared with Na^+ alone (Fig. 2). These results establish a positive correlation between the substrate-modulated F259 rotamer dynamics observed in our MD simulations and QM/MM calculations and the substrate-modulated intracellular gating dynamics measured by smFRET. Importantly, we observe that F259 dynamics and intermediate-FRET state occupancy follow the same rank order as the rates (V_{max}) of substrate transport (*SI Appendix*, Table S1). These findings support our hypothesis that F259 dynamics are allosterically coupled to intracellular gating dynamics and Na^+ release from the Na2 site.

Mutations at Position 259 That Favor the Parallel Rotamer also Stabilize the IO2 State. We next sought to test the association between F259 rotamer states and the intracellular gating dynamics

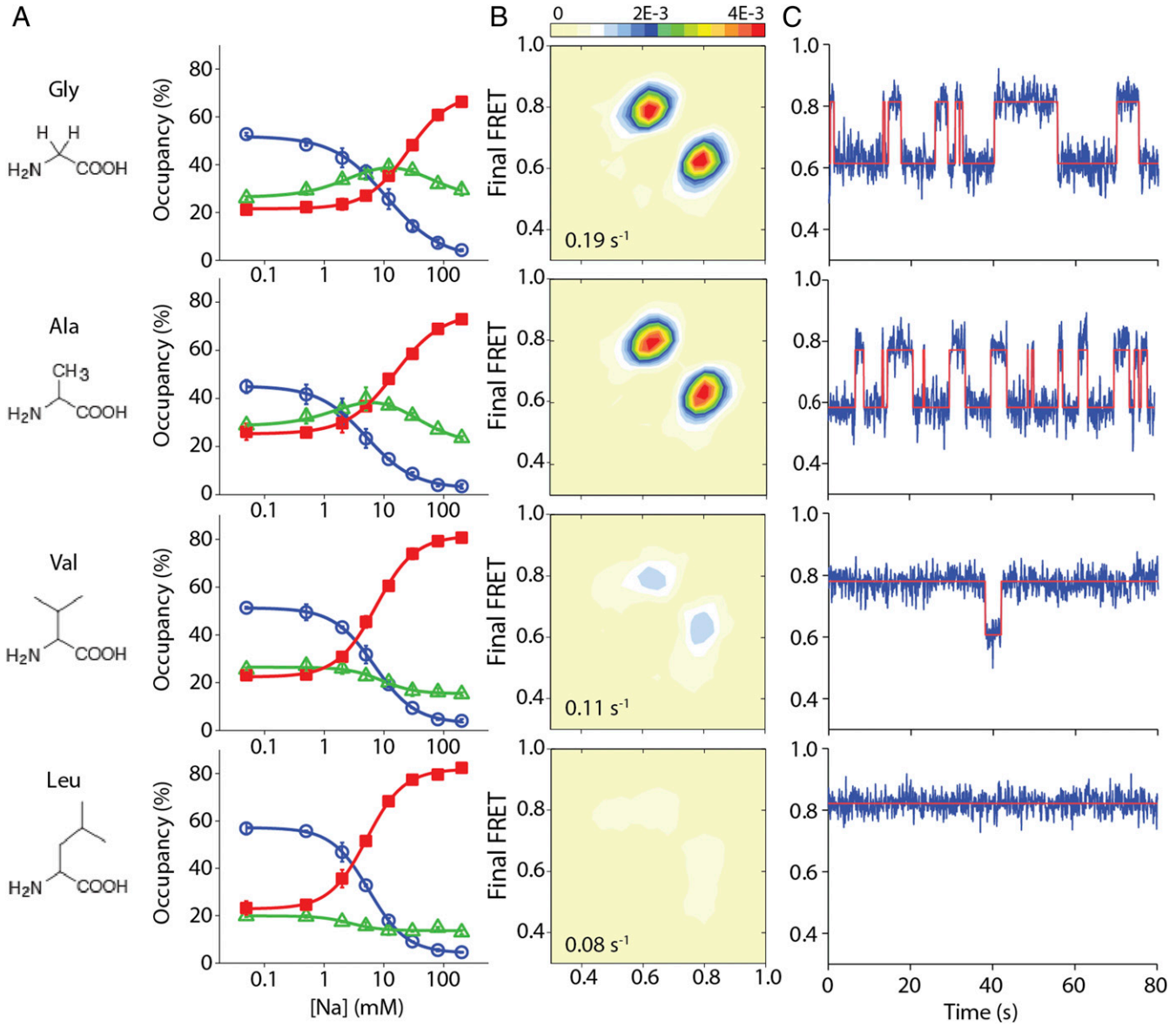

Fig. 2. Small substrates stabilize the intermediate state and induce Na^+ release. (*A*) Intracellular labeled LeuT-7C/86C was imaged using smFRET in the presence of 10 mM glycine (*Top* row), 300 μM alanine (*Top Middle*), 100 μM valine (*Bottom Middle*), and 10 μM leucine (*Bottom* row) and the indicated concentrations of Na^+. Shown are ensemble averaged occupancies in the low-FRET (blue circles), intermediate-FRET (green triangles), and high-FRET (red squares) states. Lines are fits to dose–response functions. Error bars are mean ± SD of 2 repeats. (*B*) Transition density contour plots, which show the mean FRET value in the dwell just before (bottom axis) and just after (left axis) each transition between distinct FRET states, summed into a histogram for each substrate in the presence of 30 mM Na^+. The average transition rate is given at the *Bottom Left* of each panel. Scale bar at top in transitions per histogram bin per second. (*C*) Representative FRET (blue) and state assignment (red) traces corresponding to the experiments in *B*.

observed in our smFRET experiments by constraining the rotameric state in a substrate-independent manner. Noting that the residue corresponding to F259 is a Trp in the homologous Gly transporter GlyT, and that our past homology modeling of GlyT bound to Gly positioned the tryptophan ring in the parallel state (48), we investigated the effect of a F259W mutation in LeuT. We reasoned that because substrate size affects the rotamer dynamics of F259, placing a larger residue in the substrate binding site at this position would stabilize the residue in the parallel rotameric state. We first tested this model with a 3-μs MD simulation of the LeuT-F259W in complex with Gly (Fig. 3*A*). In so doing, we found that W259 is indeed locked in the parallel state for the entire trajectory (Fig. 3*B* and *SI Appendix*, Fig. S15), while residue I359 predominantly occupied the 120° state while displaying unimpeded transitions between states (*SI Appendix*, Fig. S15). Water was also observed to transiently bridge S1 and Na2, as observed also in the Gly- and Ala-bound wild-type (LeuT-WT) simulations. Consistent with the hypothesized allosteric coupling between rotamer dynamics and intracellular gating, smFRET imaging of the F259W construct showed a stabilization of the IO2 state, a destabilization of the inward-closed state, and an increase in intracellular gating dynamics (Fig. 3 *C* and *D*). These effects, which correspond to those induced by Gly and Ala in LeuT-WT, occurred in LeuT-F259W even in the absence of substrates. These observations are consistent with the association between occupancy of the parallel rotameric state and occupancy of the IO2 state. Notably, dwells in low- and intermediate-FRET states were more clearly defined than in LeuT-WT, where transitions

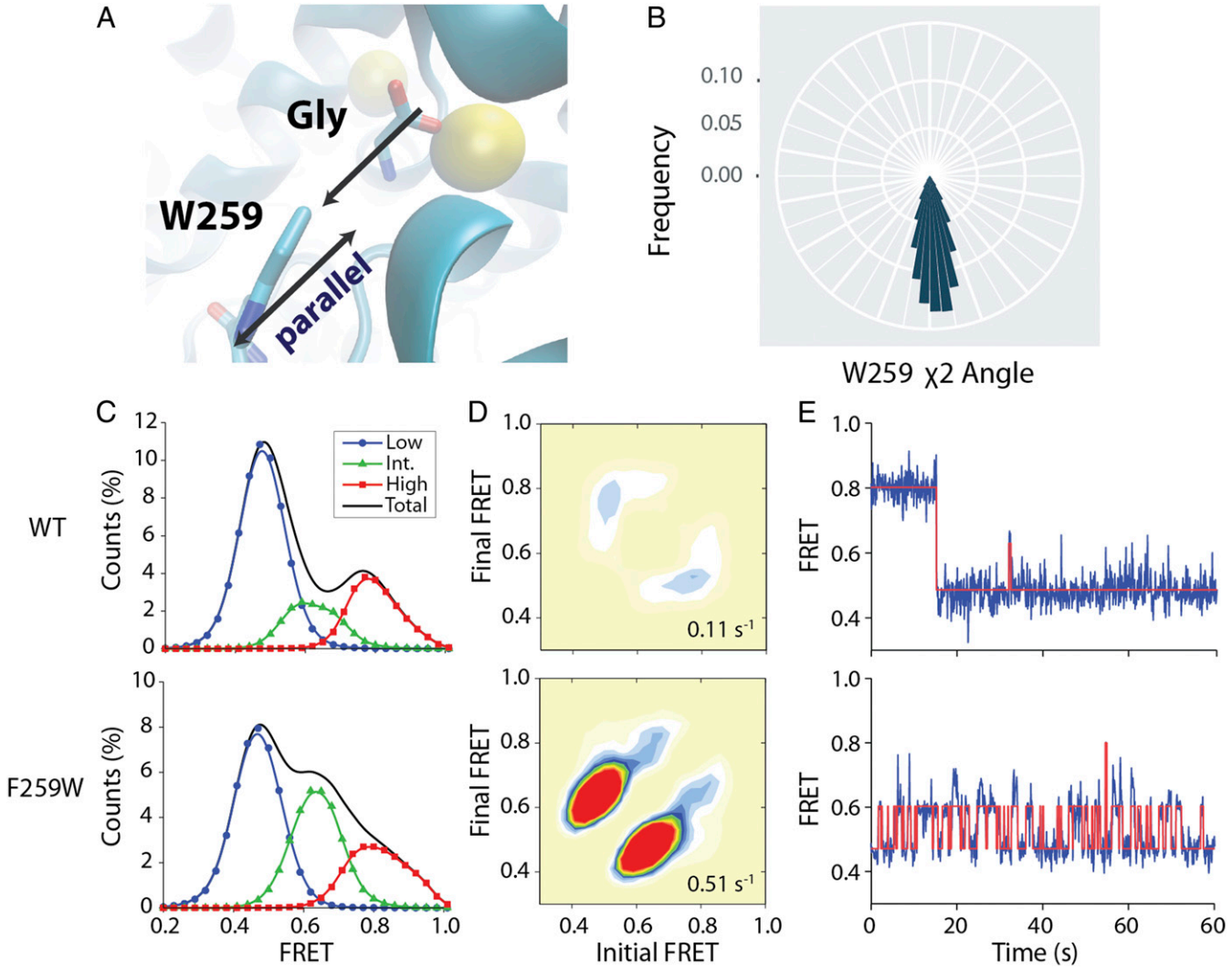

Fig. 3. The F259W mutation stabilizes the intermediate FRET state. (*A*) A representative frame of F259W from the MD simulation (depicted as in Fig. 1*A*). (*B*) Rose plot of the angular histogram of the F259 χ_2 angle, colored by angular *k*-means clustering. (*C* and *D*) LeuT-WT (*Top*) and -F259W (*Bottom*) were imaged in the absence of Na^+ and substrates. (*C*) FRET histograms for the low-FRET (blue circles), intermediate-FRET (green triangles), and high-FRET (red squares) states and total histogram (black line). (*D*) Transition density contour plots, with the average transition rate in the lower-right corner. (*E*) Example FRET (blue) and state assignment (red) traces.

between these 2 states were difficult to discern due to averaging on the imaging timescale (100 ms).

To test whether the F259W mutation affects the interaction of the transporter with Na^+, we measured $^{22}Na^+$ binding in the absence of substrate with the scintillation proximity assay. Whereas LeuT-WT exhibited an apparent 2 Na^+:1 LeuT binding stoichiometry, only 1 Na^+ molecule appeared to bind the F259W mutant (Fig. 4*A*). smFRET measurements of Na^+-induced inward closing of the F259W mutant in the absence of substrates also demonstrated significantly lower Na^+ affinity (Fig. 4*B*). The observation that Na^+ can have a very low affinity for the Na2 site is consistent with our previously reported model (23) in which Na^+ is released from the Na2 site when LeuT transitions to the IO2 state. To test directly whether the reduction of the Na^+ affinity in LeuT-F259W is caused by disrupting the integrity of the Na2 site, we made mutations that impair Na^+ binding in the Na1 (N27A) or Na2 (T354A) sites (29). Disrupting the Na2 site in the F259W background (LeuT-F259W/T354A) had only a subtle effect on the Na^+ binding affinity. In contrast, disrupting the Na1 site in the F259W background (LeuT-N27A/F259W) completely blocked Na^+ binding (Fig. 4*A*). These results suggest that Na^+ binds exclusively to the Na1 site in LeuT-F259W, supporting our model that the IO2 state corresponds to a conformation in which Na^+ has been released from the Na2 site (23). In light of our recent Markov State Model and TCF analysis of human dopamine transporter (hDAT) mechanisms, which revealed an allosteric coupling between inward-opening and Na2 release (16, 17, 37), these results suggest that the stabilization of F259 in the parallel state promotes release from Na2 through stabilization of the IO2 state.

The F259W Mutation Increases Selectivity for Gly Transport. Contrary to our model, it has been reported previously that Ala has a 4-fold greater transport rate than Gly (19). To assess the functional relevance of high basal occupancy of the IO2 state, we compared the transport rates of radiolabeled Gly and Ala by LeuT-WT and the F259W mutant. In contrast to previous findings, and in accordance with our model, we find that Gly and Ala are transported by WT LeuT with nearly equal maximal velocity (V_{max}) (*SI Appendix*, Table S1). The apparent discordance of these findings with previous uptake experiments (19, 44) may relate to the presence of a pH gradient in our investigations (i.e., $pH_{in} < pH_{out}$), which is a

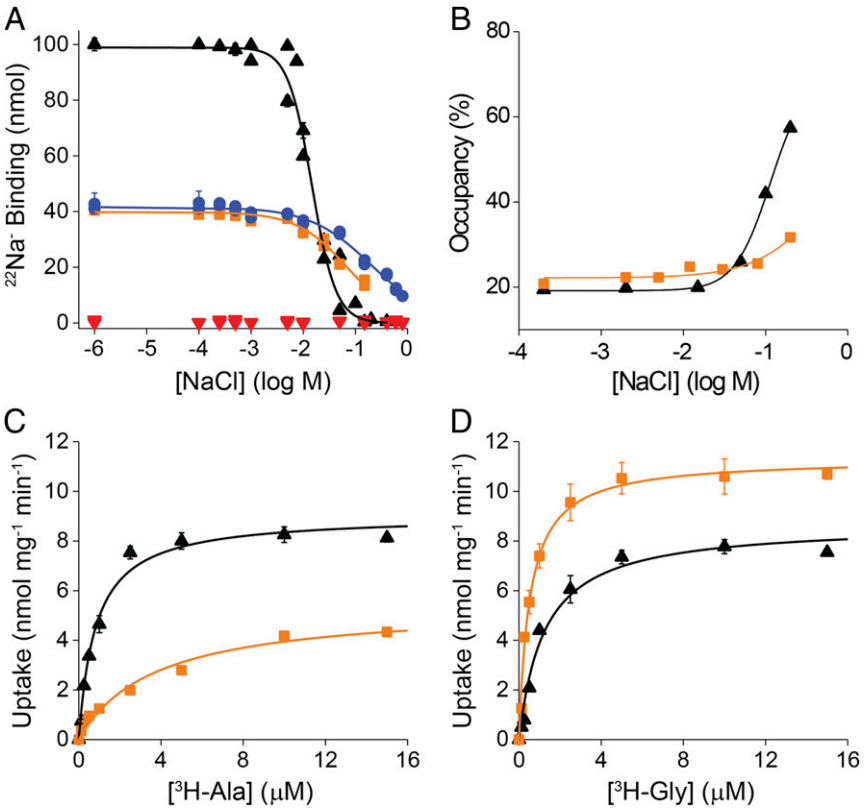

Fig. 4. Effect of the F259W mutation on Na^+ binding and substrate transport. (*A*) Na^+ binding determined by scintillation proximity assay for LeuT-WT, -F259W, -F259W/T354A, and -N27A/F259W. Binding of 50 μM [^{22}Na]Cl (50 Ci/mol) was measured in the presence of increasing concentrations of nonlabeled NaCl with 50 ng of the indicated LeuT variant. Data of ≥2 independent experiments (with technical triplicates shown as mean ± SEM) were normalized to the binding activity of LeuT-WT and plotted as function of the isotopic displacement of $^{22}Na^+$ by nonlabeled NaCl. Nonlinear regression fitting in SigmaPlot 13 was used to determine the effective concentration of 50% $^{22}Na^+$ displacement (EC_{50}) and the Hill coefficient for LeuT-WT (black triangle; 14.7 ± 0.9 mM | 1.9 ± 0.2), LeuT-F259W (orange square; 70.3 ± 5.9 mM | 0.9 ± 0.1), LeuT-F259W/T354A (open blue circles; 201.2 ± 17.1 mM | 0.7 ± 0.1), and LeuT-N27A/F259W (red triangles). (*B*) Ensemble averaged occupancy in the high-FRET state from experiments imaging LeuT-WT (black triangles) and -F259W (orange squares) in the absence of substrates and the presence of the indicated concentrations of Na^+. Lines are fits to dose–response functions with EC_{50} values of ∼110 mM (WT) and >200 mM (F259W). (*C* and *D*) Uptake of ^{3}H-Ala (*C*) or ^{3}H-Gly (*D*) by proteoliposomes containing LeuT-WT or -F259W. Uptake was performed in Tris-Mes, pH 8.5, containing 50 mM (LeuT-WT) or 800 mM (-F259W) NaCl (equimolarly replaced with Tris/Mes) using proteoliposomes with an internal pH of 6.5 (17). The individual uptake data of 2 independent experiments (with technical triplicates) were averaged and shown as mean ± SEM and plotted as function of the substrate concentration. Data were subjected to Michaelis–Menten fitting in SigmaPlot 13 to calculate the V_{max} and K_m of LeuT-WT for Ala (9.0 ± 0.3 nmol × mg^{-1} × min^{-1} | 0.8 ± 0.1 μM) and Gly (8.7 ± 0.4 nmol × mg^{-1} × min^{-1} | 1.2 ± 0.2 μM) and of LeuT-F259W for Ala (5.4 ± 0.5 nmol × mg^{-1} × min^{-1} | 3.7 ± 0.9 μM) and Gly (11.3 ± 0.3 nmol × mg^{-1} × min^{-1} | 0.5 ± 0.06 μM).

critical component needed for optimal uptake measurements for LeuT and other Cl^--independent bacterial NSS homologs that feature H^+ extrusion as part of the Na^+/substrate symport reaction (49–52). The F259W mutation was found to increase the K_m and decrease the V_{max} of Ala transport, leading to substantially diminished transport activity for this prototypical LeuT substrate (Fig. 4*C*). This observation is consistent with the idea that the increased steric occupancy of the binding site by W259, in combination with the Ala substrate, mimics that observed for the larger substrates in the WT LeuT. In contrast, the K_m for Gly was decreased substantially and the V_{max} was increased compared with WT (Fig. 4*D*). Based on the present findings, we therefore conclude that the F259W mutation is sufficient to increase the selectivity of LeuT for Gly transport. These results are consistent with recently published findings that the reverse mutation in GlyT transformed the normally selective transporter into a nonselective amino acid transporter (53).

Discussion

The present findings reveal a mechanism by which substrate selectivity is achieved in the function of the NSS homolog LeuT. Our previous NbIT analysis (24) predicted that residues F259 and I359 serve as the main mediators of allosteric communication between the substrate in the S1 site and the intracellular gate. Here, we used a combination of MD simulations, QM/MM calculations, smFRET imaging, and Na^+ binding assays to find that the mode of interaction of substrates with residues F259 and I359 elicits substrate-specific allosteric modulation of both intracellular gating and Na^+ release from the Na2 site. In this allosteric mechanism, F259 acts in a manner analogous to a volumetric sensor of substrate bulk. Low-volume substrates that bind while allowing free rotation of F259 induce rapid sampling of an inward-facing, intermediate-FRET state (IO2) associated with the release of Na^+ from the Na2 binding site. In contrast, bulky substrates that act sterically to prevent the rotation of F259 stabilize a perpendicular F259 rotamer state and the fully Na^+-bound inward-closed state. We show that, in the absence of substrate and in the presence of the low-volume Gly, the F259W mutation fixes the residue in the parallel rotameric state and induces rapid sampling and high occupancy of the IO2 state. In the IO2 state, the affinity of Na^+ in the Na2 site is drastically reduced even in the absence of substrate. Together, these results suggest that, in the case of F259, occupancy of the parallel state is necessary and sufficient to achieve the IO2 state associated with rapid substrate

transport (23). While the atomic-level structural details of the IO2 state are still unresolved for LeuT, the predictive power of our previous simulations of this process in hDAT (16, 17, 37) suggests that the major components will be similar.

We note, however, that the relationship between apparent intermediate state occupancy and transport rates (V_{max}) is not linear. Val is transported much more rapidly than Leu, but partially stabilizes the inward-closed state while destabilizing the parallel F259 rotamer, albeit to a lesser extent than Leu. However, we do observe that, in the presence of bound Val, while the parallel F259 state is not metastable, it is occupied transiently as a necessary pseudotransition state when F259 exchanges between perpendicular states (see small populations in Fig. 1*B* and significant transition density of perpendicular to parallel and parallel to perpendicular transitions in *SI Appendix*, Fig. S7). In line with the proposal that occupancy of the F259 parallel state is necessary for stabilization of the IO2 state, these transient occupations may increase the occupancy of the IO2 state, but not to the extent that it becomes metastable on the timescale of the smFRET experiments. It should also be noted that the involvement of S2 in the Na^+ release process is likely to also be substrate dependent (9), and the interaction between S1- and S2-dependent modulation of Na2 affinity cannot be separated in our experiments.

The smFRET imaging results described here gain additional perspective from recent site-directed fluorescence quenching spectroscopy (SDFQS) experiments (44) that provided evidence for substrate-induced conformational changes in LeuT. Specifically, an increase in solvent accessibility of a fluorophore inserted at the intracellular end of TM5 was observed upon binding of all transported substrates, but not binding of inhibitors or Na^+ alone. In this context, we note that the fluorophores used and labeling pattern employed in our smFRET experiments were specifically chosen to avoid environmental impacts. Correspondingly, solvent accessibility changes resulting from conformational changes in the protein may not be detected unless they were also accompanied by significant changes in interfluorophore distance. Nonetheless, the SDFQS experiments showed a substrate-dependent decrease in fluorophore solvent accessibility that correlated with substrate size and transport rates. Moreover, the rank order of these effects was the same as observed here for the F259 rotamer dynamics, the related IO2 state stabilization, and the increase in intracellular dynamics. Thus, the modulation of accessibility observed with SDFQS may well arise from the increased occupancy of the IO2 state observed with the more rapidly transported substrates, or to mechanistically related processes.

In view of the determining role of F259 interactions with substrates demonstrated here, the conservation of F259 across the synaptic monoamine transporters (sMATs) becomes critical to consider. Because the dopamine, norepinephrine, and serotonin transporters (DAT, NET, and SERT, respectively) all transport substrates with bulky ring substituents, it may be expected that the residue homologous to F259 in each of these transporters would engage these substrates in a manner that would inhibit transport. While comparison of X-ray structures of *Drosophila* DAT (dDAT) (54–56) in the presence of various S1 ligands indicate that the corresponding F325 can sample distinct states similar to the parallel and perpendicular states observed in our MD simulations of LeuT, extant structural data do not reveal a clear correlation between the F325 rotamer state and the bound ligands in dDAT. In dDAT crystal structures, which are all in either an occluded or outward-facing open state, the F325 residue is in a perpendicular state when interacting with either the endogenous substrate dopamine or the inhibitor cocaine (56), while nisoxetine, a selective NET inhibitor in humans that also binds to and inhibits dDAT, contacts F325 with 1 of its rings to stabilize a parallel-like state of F325 (54). Regarding the possibility that crystallographic conditions could be responsible for the stabilization of F325 in a particular state in the dopamine-bound structure, similar to what we reasoned above based on the QM/MM calculations on the LeuT X-ray structures, we note that in this case significant occupancy of the parallel state was also not seen in our extensive MD simulations of inward-opening in dDAT and the human homolog hDAT (16, 17, 37). This observation suggests that, in DAT, dopamine does in fact stabilize the perpendicular state regardless of intracellular gating configuration. This inference is consistent with the transfer of the mechanism of regulation of inward opening and Na2 release in eukaryotic transporters to the intracellular N terminus, as described recently (57). In X-ray structures of human SERT (hSERT) (58, 59) bound to the antidepressant inhibitors paroxetine and (*S*)-citalopram (58), the corresponding F341 is significantly displaced from its position in LeuT and dDAT, as it is situated below the inhibitors with the ring in a perpendicular-like state. In hSERT, in complex with sertraline and fluvoxamine (59), F341 exhibits a parallel-like state. Notably, no structure of SERT with substrate has been published to date, perhaps reflecting the dynamic nature of this state anticipated by our smFRET measurements of LeuT. The influence of inhibitors on the χ_1 angle of F341 has recently been associated with inhibitor affinity (60). The diverse conformational space sampled by this conserved phenylalanine in published sMAT X-ray structures may indicate that the mechanistic role it plays in substrate transport in LeuT is not strictly conserved across the sMATs but has evolved to require an interplay with other structural elements (54). In view of its conservation, however, the predicted role of this residue in the function of this important transporter family warrants further investigation, as the design of inhibitors that specifically act via the inhibition of the Na^+ release step could lead to the development of future antidepressants and psychostimulants.

Methods

MD Simulations. The X-ray structure of LeuT from PDB ID 3F3E (19) was used for all atomistic MD simulations. Short loop fragments (residues 1 to 4 and 132 to 134), not resolved crystallographically, were built and added to the X-ray structure using Modeler (61). To build Ala-, Val-, and Gly-bound LeuT models, the substrate Leu in the 3F3E structure was substituted by the respective ligands using the Mutator plug-in within VMD (62). Using the CHARMM-GUI web server (63), the LeuT models were embedded in a membrane with 75:25 mixture of 1-palmitoyl-2-oleoyl-*sn*-glycero-3-phosphoethanolamine (POPE)/1-palmitoyl-2-oleoyl-*sn*-glycero-3-phospho-(1′-*rac*-glycerol) (POPG) lipids (296 lipids in total), hydrated and ionized with 0.15 M Na^+Cl^- salt, resulting in the final system size of ∼118,000 atoms (including hydrogen atoms).

All of the molecular systems assembled were first subjected to a multistep equilibration protocol (for examples, see refs. 16 and 37) with NAMD, version 2.9, using CHARMM36 parameters for proteins (64), lipids (65), and ions. Briefly, this phase included the following: 1) minimization for 5,000 steps and running MD with 1-fs integration time step for 250 ps, fixing all atoms in the system except for the lipid tails; 2) minimization for 2,500 steps and performing MD with 1-fs time step for 500 ps with constrained protein backbone and lipid headgroups [force constant of 1 kcal/(mol·Å^2)] and keeping water out of the membrane hydrophobic core; 3) gradual release of the constraints on the protein backbone and lipid headgroup atoms [force constant of 0.5 and 0.1 kcal/(mol·Å^2)] while still keeping water out of the membrane interior. At each value of the force constant, the system was minimized for 2,500 steps followed by 500-ps MD (with 1-fs time step); 4) unbiased MD simulation for 30 ns using 2-fs time step. These steps implemented PME for electrostatics interactions (66) and were carried out in the NPT ensemble under semiisotropic pressure coupling conditions, at 310 K temperature. The Nosé–Hoover Langevin piston (67) algorithm was used to control the target $P = 1$ atm pressure with the *LangevinPistonPeriod* set to 100 fs and *LangevinPistonDecay* set to 50 fs. The van der Waals interactions were calculated applying a cutoff distance of 12 Å and switching the potential from 10 Å. After this initial phase, the molecular systems were subjected to 3-μs-long MD simulations on Anton1, a special-purpose supercomputer machine (68). These production runs implemented the same set of CHARMM36 force-field parameters and were carried out in the NPT ensemble under semiisotropic pressure coupling conditions [using the Multigrator scheme that employs the Martyna–Tuckerman–Klein barostat (69)

and the Nosé–Hoover thermostat (70)], at 310 K temperature, with 2-fs time step, and using PME for electrostatic interactions. All of the other run parameters were derived from the Anton guesser scripts based on the system chemistry.

A representative frame from the Anton trajectory of Gly-bound LeuT in which the F259 ring assumed the parallel state (*Results*) was chosen to mutate the F259 residue into Trp (F259W) using the Mutator plug-in in VMD. The resulting molecular system was minimized and ran with unbiased MD for 30 ns using NAMD 2.9 after which it was transferred to Anton1 for 3 ms of MD simulation.

Hybrid QM/MM. QM/MM calculations scanning the angle spaces of F259 and I359 were performed using the QSite program from version 2017-2 of Maestro from Schrödinger (71). To maintain consistency with the MD simulations, the protein models were prepared from the same structure (19). Structures for the glycine-, alanine-, and valine-bound LeuT were prepared by mutating the bound leucine in Maestro. The QM portion of the calculations was performed using the density functional theory method DFT-B3LYP (72, 73) with the LACVP* basis set. The QM region in all cases included the bound ligand, F259, I359, and the side chain of the scanned residue's 2 immediate neighbors in sequence (G258, F259, F260, and the side chain of I359 when F259 was scanned; A358, I359, M360, and the side chain of F259 when I359 was scanned). The MM region was comprised of the rest of the protein, with the backbone atoms constrained using a 25.00 kcal/(mol·Å^2) harmonic force constant. At the QM/MM interface, the frozen orbital method was used. Convergence of MM minimization steps was based on an energy change criterion of 10^{-7} kcal/mol and a gradient change criterion of 0.01 kcal/(mol·Å), using a truncated Newton algorithm, and a maximum of 1,000 cycles. After an initial minimization step, the dihedral being scanned (F259 χ_2 and I359 χ_1) was rotated a total 1,080° in steps of 5°. The initial dihedral was based on that of the crystal structure (81.612° for F259 χ_2; 226.799° for I359 χ_1).

Identification of the F259 Rotameric States. To characterize the F259 rotameric state, we calculated the dihedral angle formed by the Cα, Cβ, Cγ, and CD1 carbons across each MD trajectory. As we introduced new substrates into the S1 binding sites, the initial dynamics of the binding site residues are expected to be far from equilibrium. We used a recently developed method (74), adapted for angular data, to determine how much of the initial portion of the trajectories should be discarded. In the analysis, the first *t*0 frames are discarded, where *t*0 is chosen such that the effective number of observations remaining after correcting for autocorrelation is maximized. To calculate autocorrelation in the angular data, the time-lagged circular correlation C_t is used:

$$C_t = \frac{\sum_{i=1}^{T-t} \sin(\theta_i - \langle\theta\rangle)\sin(\theta_{i+t} - \langle\theta\rangle)}{\sqrt{\sum_{i=1}^{T-t} \sin^2(\theta_i - \langle\theta\rangle)\sum_{i=1}^{T-t} \sin^2(\theta_{i+t} - \langle\theta\rangle)}}. \quad [1]$$

After removing the nonequilibrium portions of the trajectories (*SI Appendix*, Figs. S1–S5), we performed *k*-centroids clustering using the kcca function in the flexclust package in R (75) to identify the rotameric states. The angular histograms of the glycine- and alanine-bound simulations revealed 4 distinct states, and thus the number of clusters, *k*, was chosen to be 4 and clustering was performed using a modified *k*-means algorithm that minimizes the angle between cluster members and the standardized mean of the cluster. We clustered the angle distributions from the glycine-bound trajectory, which sampled all 4 states equally, and then used the resulting centroids and to cluster the alanine-, valine-, leucine-, and F259W glycine-bound angle distributions.

Protein Expression and Purification for smFRET Experiments. LeuT constructs were expressed and purified as described previously (23). Briefly, LeuT was expressed in *Escherichia coli* using pQO18-TEV vector derivatives with the H7C/R86C mutations or H7C/R86C/F259W as previously described (21). The constructs were solubilized in *n*-dodecyl β-D-maltopyranoside (DDM), purified by immobilized metal affinity chelate chromatography using a Ni^{2+} Sepharose 6 FastFlow column (GE Healthcare), and then labeled with maleimide-activated LD550 and LD650 fluorophores (Lumidyne Technologies) at a 1:1.5 molar ratio (200 μM total) for 1 h at 4 °C, followed by size exclusion chromatography using a Superdex 200 16/60 column.

smFRET Imaging Experiments. smFRET imagine experiments were performed using a prism-based total internal reflection fluorescence microscope as previously described (21–23, 34). Passivated microfluidic imaging chambers were prepared with 0.8 μM streptavidin (Invitrogen) and 4 nM biotin-tris-(NTA-Ni^{2+}) (76) and fluorophore-labeled, His-tagged LeuT molecules were reversibly surface immobilized. LD550 fluorophores were excited by the evanescent wave generated by total internal reflection of a single-frequency light source (Opus 532; Laser Quantum). Photons emitted from LD550 and LD650 were collected using a 1.27 numerical aperture, 60× water-immersion objective (Nikon) and a MultiCam-LS device (Cairn) with a T635lpxr-UF2 dichroic mirror to separate the spectral channels onto 2 synchronized sCMOS cameras (Flash 4.0, version 2; Hamamatsu). Fluorescence data were acquired at 10 frames per second (100-ms time resolution) using custom software implemented in LabView (National Instruments).

All experiments were performed in buffer containing 50 mM Tris/Mes (pH 7.0), 10% glycerol, 0.02% (wt/vol) DDM (Anagrade; Anatrace), 1 mM 2-mercaptoethanol, and 200 mM total salt (NaCl and KCl, as specified). An oxygen-scavenging environment containing 0.2 unit per mL glucose oxidase (Sigma; G2133), 1.8 units per μL catalase (Sigma; C40), 0.1% (vol/vol) glucose was employed to minimize photobleaching. Both enzymes were purified by gel filtration using a Superdex 200 13/30 column (GE Healthcare) before use. All experiments were performed at 25 °C.

Analysis of smFRET data were performed using SPARTAN, freely available smFRET analysis software written in MATLAB (MathWorks) (34), as previously described (23). Spectral bleed-through from the donor to the acceptor channel was corrected by subtracting a set fraction (0.165) of the donor intensity from the acceptor. The FRET efficiency was calculated as follows: $EFRET = IA/(IA + ID)$, where *IA* and *ID* are the donor and acceptor fluorescence traces and *EFRET* is set to zero whenever the donor was in the dark state. A subset of the acquired traces was selected for further analysis using the following criteria: 1) single-step donor photobleaching, 2) SNRBackground ≥ 15, 3) SNRSignal ≥ 4, 4) <4 donor blinking events, and 5) FRET efficiency above 0.15 for at least 300 frames (30 s). Replicates (*n*) are defined as data acquired from independent immobilizations of LeuT, generally performed on separate days with newly prepared buffer solutions and frozen aliquots obtained from a single preparation. Finally, traces were fit to a three-state model using the segmental *k*-means algorithm (77) as described previously (23).

Radiotracer-Based Binding and Transport Studies. Plasmid-encoded LeuT variants were produced in *E. coli* C43(DE3) and purified as described previously (9). Direct binding of 50 μM [$^{22}Na^+$]Cl (50 Ci/mol) by 50 ng of purified and desalted protein was measured with the scintillation proximity assay (SPA) as described (9, 78) in assay buffer composed of 100 to 900 mM Tris/Mes, pH 7.5/0 to 800 mM NaCl (equimolar substitution of NaCl with Tris/Mes)/20% glycerol/0.1 mM TCEP/0.1% DDM using 1.25 mg/mL copper His-tag PVT SPA beads (Perkin-Elmer). Total binding was corrected for the non–proximity-based signal to determine the specific binding activity of each LeuT variant, and data were normalized to the maximal binding observed for LeuT-WT that was assayed in parallel in all individual measurements. Data of ≥2 independent experiments shown as mean ± SEM of triplicate determinations were subjected to global fitting in SigmaPlot 13 to determine the kinetic constants (the error indicates the SEM).

Transport of [^{3}H]Ala (56 Ci/mmol) or [^{3}H]Gly (60 Ci/mmol) or [^{3}H]valine (60 Ci/mmol), or [^{3}H]Leu (100 Ci/mmol) (all from American Radiolabeled Chemicals) was measured in proteoliposomes containing the indicated LeuT variant that was incorporated in preformed liposomes composed of *E. coli* polar lipids and POPC [3:1 (wt/wt)] at a protein-to-lipid ratio of 1:150 (wt/wt) as described (9). Uptake of the radiolabeled amino acid was performed in 850 mM Tris/Mes, pH 8.5/50 mM NaCl (for LeuT-WT) or 100 mM Tris/Mes, pH 8.5/800 mM NaCl (for LeuT-F259W) and samples were filtered through 0.45-μm membrane filters (EMD Millipore) on a rapid filtration station (9). Data of 2 independent experiments performed in triplicate were plotted and analyzed in SigmaPlot 13, and the Michaelis–Menten transport constant (K_m) and maximum velocity (V_{max}) were obtained with nonlinear regression fitting using the Michaelis–Menten model. The amount of LeuT incorporated into the proteoliposomes was determined using densiometric quantification of samples subjected to 11% SDS/PAGE followed by silver staining of the proteins using the ImageJ software (NIH). Known amounts of LeuT [determined with the Amidoblack Protein Assay (79)] served as calibration standards.

ACKNOWLEDGMENTS. We thank Roger Altman for preparation of microfluidic chambers, Derek Shore for his help with setting up the QM/MM calculations, and the members of the S.C.B., J.A.J., and H.W. laboratories for helpful discussions. This research was supported by NIH Grants R21 MH099491

(S.C.B.), U54 GM087510 (S.C.B., J.A.J., and H.W.), P01 DA012408 (H.W.), R01 DA041510 (J.A.J., H.W., and S.C.B.), and F31 DA035533 (M.V.L.). Computational results in this work were carried out at resources of the Oak Ridge Leadership Computing Facility (Advanced Scientific Computing Research Leadership Computing Challenge Allocation BIP109) at the Oak Ridge National Laboratory and an allocation at the National Energy Research Scientific Computing Center (Repository m1710), each supported by the Office of Science of the US Department of Energy under Contracts DE-AC05-00OR22725 and DE-AC02-05CH11231, respectively; the Extreme Science and Engineering Discovery Environment (Account TG-MCB120008), which is supported by National Science Foundation Grant ACI-1053575; and the Anton 2 supercomputer provided by D. E. Shaw Research at the Pittsburgh Supercomputing Center through NIH Grant R01 GM116961. The computational resources of the David A. Cofrin Center for Biomedical Information in the HRH Prince Alwaleed Bin Talal Bin Abdulaziz Alsaud Institute for Computational Biomedicine at Weill Cornell Medicine are gratefully acknowledged.

1. M. V. LeVine, M. A. Cuendet, G. Khelashvili, H. Weinstein, Allosteric mechanisms of molecular machines at the membrane: Transport by sodium-coupled symporters. *Chem. Rev.* **116**, 6552–6587 (2016).
2. L. Iversen, Neurotransmitter transporters and their impact on the development of psychopharmacology. *Br. J. Pharmacol.* **147** (suppl. 1), S82–S88 (2006).
3. S. G. Amara, M. S. Sonders, Neurotransmitter transporters as molecular targets for addictive drugs. *Drug Alcohol Depend.* **51**, 87–96 (1998).
4. O. Jardetzky, Simple allosteric model for membrane pumps. *Nature* **211**, 969–970 (1966).
5. Y. Shi, Common folds and transport mechanisms of secondary active transporters. *Annu. Rev. Biophys.* **42**, 51–72 (2013).
6. S. Stolzenberg *et al*., The role of transmembrane segment 5 (TM5) in Na2 release and the conformational transition of neurotransmitter:sodium symporters toward the inward-open state. *J. Biol. Chem.* **292**, 7372–7384 (2017).
7. H. Koldsø *et al*., Unbiased simulations reveal the inward-facing conformation of the human serotonin transporter and Na^+ ion release. *PLoS Comput. Biol.* **7**, e1002246 (2011).
8. J. Kniazeff *et al*., An intracellular interaction network regulates conformational transitions in the dopamine transporter. *J. Biol. Chem.* **283**, 17691–17701 (2008).
9. L. Shi, M. Quick, Y. Zhao, H. Weinstein, J. A. Javitch, The mechanism of a neurotransmitter:sodium symporter—inward release of Na^+ and substrate is triggered by substrate in a second binding site. *Mol. Cell* **30**, 667–677 (2008).
10. S. Bracher *et al*., Glu-311 in external loop 4 of the sodium/proline transporter PutP is crucial for external gate closure. *J. Biol. Chem.* **291**, 4998–5008 (2016).
11. M. H. Cheng, J. Garcia-Olivares, S. Wasserman, J. DiPietro, I. Bahar, Allosteric modulation of human dopamine transporter activity under conditions promoting its dimerization. *J. Biol. Chem.* **292**, 12471–12482 (2017).
12. A. Paz *et al*., Conformational transitions of the sodium-dependent sugar transporter, vSGLT. *Proc. Natl. Acad. Sci. U.S.A.* **115**, E2742–E2751 (2018).
13. J. Li, P. C. Wen, M. Moradi, E. Tajkhorshid, Computational characterization of structural dynamics underlying function in active membrane transporters. *Curr. Opin. Struct. Biol.* **31**, 96–105 (2015).
14. S. C. Peng *et al*., Computational modeling with forward and reverse engineering links signaling network and genomic regulatory responses: NF-kappaB signaling-induced gene expression responses in inflammation. *BMC Bioinformatics* **11**, 308 (2010).
15. N. Akyuz *et al*., Transport domain unlocking sets the uptake rate of an aspartate transporter. *Nature* **518**, 68–73 (2015).
16. G. Khelashvili *et al*., Spontaneous inward opening of the dopamine transporter is triggered by PIP2-regulated dynamics of the N-terminus. *ACS Chem. Neurosci.* **6**, 1825–1837 (2015).
17. M. V. LeVine, M. A. Cuendet, A. M. Razavi, G. Khelashvili, H. Weinstein, Thermodynamic coupling function analysis of allosteric mechanisms in the human dopamine transporter. *Biophys. J.* **114**, 10–14 (2018).
18. A. Yamashita, S. K. Singh, T. Kawate, Y. Jin, E. Gouaux, Crystal structure of a bacterial homologue of Na^+/Cl^--dependent neurotransmitter transporters. *Nature* **437**, 215–223 (2005).
19. S. K. Singh, C.L. Piscitelli, A. Yamashita, E. Gouaux, A competitive inhibitor traps LeuT in an open-to-out conformation. *Science* **322**, 1655–1661 (2008).
20. H. Krishnamurthy, C. L. Piscitelli, E. Gouaux, Unlocking the molecular secrets of sodium-coupled transporters. *Nature* **459**, 347–355 (2009).
21. Y. Zhao *et al*., Single-molecule dynamics of gating in a neurotransmitter transporter homologue. *Nature* **465**, 188–193 (2010).
22. Y. Zhao *et al*., Substrate-modulated gating dynamics in a Na^+-coupled neurotransmitter transporter homologue. *Nature* **474**, 109–113 (2011).
23. D. S. Terry *et al*., A partially-open inward-facing intermediate conformation of LeuT is associated with Na^+ release and substrate transport. *Nat. Commun.* **9**, 230 (2018).
24. M. V. LeVine, H. Weinstein, NbIT—a new information theory-based analysis of allosteric mechanisms reveals residues that underlie function in the leucine transporter LeuT. *PLoS Comput. Biol.* **10**, e1003603 (2014).
25. K. Kazmier *et al*., Conformational dynamics of ligand-dependent alternating access in LeuT. *Nat. Struct. Mol. Biol.* **21**, 472–479 (2014).
26. C. Zhao *et al*., Ion-controlled conformational dynamics in the outward-open transition from an occluded state of LeuT. *Biophys. J.* **103**, 878–888 (2012).
27. H. Krishnamurthy, E. Gouaux, X-ray structures of LeuT in substrate-free outward-open and apo inward-open states. *Nature* **481**, 469–474 (2012).
28. M. H. Cheng, I. Bahar, Coupled global and local changes direct substrate translocation by neurotransmitter-sodium symporter ortholog LeuT. *Biophys. J.* **105**, 630–639 (2013).
29. S. Tavoulari *et al*., Two Na^+ sites control conformational change in a neurotransmitter transporter homolog. *J. Biol. Chem.* **291**, 1456–1471 (2016).
30. S. Adhikary *et al*., Conformational dynamics of a neurotransmitter:sodium symporter in a lipid bilayer. *Proc. Natl. Acad. Sci. U.S.A.* **114**, E1786–E1795 (2017).
31. K. Kazmier, S. Sharma, S. M. Islam, B. Roux, H. S. Mchaourab, Conformational cycle and ion-coupling mechanism of the Na^+/hydantoin transporter Mhp1. *Proc. Natl. Acad. Sci. U.S.A.* **111**, 14752–14757 (2014).
32. Z. Li *et al*., Identification of a second substrate-binding site in solute-sodium symporters. *J. Biol. Chem.* **290**, 127–141 (2015).
33. M. Quick *et al*., The LeuT-fold neurotransmitter:sodium symporter MhsT has two substrate sites. *Proc. Natl. Acad. Sci. U.S.A.* **115**, E7924–E7931 (2018).
34. M. F. Juette *et al*., Single-molecule imaging of non-equilibrium molecular ensembles on the millisecond timescale. *Nat. Methods* **13**, 341–344 (2016).
35. Q. Zheng *et al*., Ultra-stable organic fluorophores for single-molecule research. *Chem. Soc. Rev.* **43**, 1044–1056 (2014).
36. M. F. Juette *et al*., The bright future of single-molecule fluorescence imaging. *Curr. Opin. Chem. Biol.* **20**, 103–111 (2014).
37. A. M. Razavi, G. Khelashvili, H. Weinstein, A Markov state-based quantitative kinetic model of sodium release from the dopamine transporter. *Sci. Rep.* **7**, 40076 (2017).
38. M. V. LeVine, J. Perez-Aguilar, H. Weinstein, "N-body information theory (NbIT) analysis of rigid-body dynamics in intracellular loop 2 of the 5-HT2A receptor." *Proceedings of IWWBIO 2014*, F. Ortuño, Rojas, I., Eds. (Copicentro Granada), pp. 1190–1201 (2014).
39. M. A. Cuendet, H. Weinstein, M. V. LeVine, The allostery landscape: Quantifying thermodynamic couplings in biomolecular systems. *J. Chem. Theory Comput.* **12**, 5758–5767 (2016).
40. A. Sethi, J. Eargle, A. A. Black, Z. Luthey-Schulten, Dynamical networks in tRNA:protein complexes. *Proc. Natl. Acad. Sci. U.S.A.* **106**, 6620–6625 (2009).
41. A. Pandini, A. Fornili, F. Fraternali, J. Kleinjung, Detection of allosteric signal transmission by information-theoretic analysis of protein dynamics. *FASEB J.* **26**, 868–881 (2012).
42. A. del Sol, H. Fujihashi, D. Amoros, R. Nussinov, Residues crucial for maintaining short paths in network communication mediate signaling in proteins. *Mol. Syst. Biol.* **2**, 0019 (2006).
43. S. Stolzenberg, M. Michino, M. V. Levine, H. Weinstein, L. Shi, Computational approaches to detect allosteric pathways in transmembrane molecular machines. *Biochim. Biophys. Acta Biomembr.* **1858**, 1652–1662 (2016).
44. C. B. Billesbølle *et al*., Substrate-induced unlocking of the inner gate determines the catalytic efficiency of a neurotransmitter:sodium symporter. *J. Biol. Chem.* **290**, 26725–26738 (2015).
45. M. V. LeVine, H. Weinstein, AIM for allostery: Using the Ising model to understand information processing and transmission in allosteric biomolecular systems. *Entropy (Basel)* **17**, 2895–2918 (2015).
46. C. Zhao, S. Y. Noskov, The role of local hydration and hydrogen-bonding dynamics in ion and solute release from ion-coupled secondary transporters. *Biochemistry* **50**, 1848–1856 (2011).
47. H. Schrauber, F. Eisenhaber, P. Argos, Rotamers: To be or not to be? An analysis of amino acid side-chain conformations in globular proteins. *J. Mol. Biol.* **230**, 592–612 (1993).
48. T. Beuming, L. Shi, J. A. Javitch, H. Weinstein, A comprehensive structure-based alignment of prokaryotic and eukaryotic neurotransmitter/Na^+ symporters (NSS) aids in the use of the LeuT structure to probe NSS structure and function. *Mol. Pharmacol.* **70**, 1630–1642 (2006).
49. M. Quick *et al*., State-dependent conformations of the translocation pathway in the tyrosine transporter Tyt1, a novel neurotransmitter:sodium symporter from *Fusobacterium nucleatum*. *J. Biol. Chem.* **281**, 26444–26454 (2006).
50. E. Zomot *et al*., Mechanism of chloride interaction with neurotransmitter:sodium symporters. *Nature* **449**, 726–730 (2007).
51. Y. Zhao *et al*., Substrate-dependent proton antiport in neurotransmitter:sodium symporters. *Nat. Chem. Biol.* **6**, 109–116 (2010).
52. A. K. Kantcheva *et al*., Chloride binding site of neurotransmitter sodium symporters. *Proc. Natl. Acad. Sci. U.S.A.* **110**, 8489–8494 (2013).
53. J. E. Carland *et al*., Molecular determinants for substrate interactions with the glycine transporter GlyT2. *ACS Chem. Neurosci.* **9**, 603–614 (2017).
54. A. Penmatsa, K. H. Wang, E. Gouaux, X-ray structures of *Drosophila* dopamine transporter in complex with nisoxetine and reboxetine. *Nat. Struct. Mol. Biol.* **22**, 506–508 (2015).
55. A. Penmatsa, K. H. Wang, E. Gouaux, X-ray structure of dopamine transporter elucidates antidepressant mechanism. *Nature* **503**, 85–90 (2013).
56. K. H. Wang, A. Penmatsa, E. Gouaux, Neurotransmitter and psychostimulant recognition by the dopamine transporter. *Nature* **521**, 322–327 (2015).
57. A. M. Razavi, G. Khelashvili, H. Weinstein, How structural elements evolving from bacterial to human SLC6 transporters enabled new functional properties. *BMC Biol.* **16**, 31 (2018).
58. J. A. Coleman, E. M. Green, E. Gouaux, X-ray structures and mechanism of the human serotonin transporter. *Nature* **532**, 334–339 (2016).
59. J. A. Coleman, E. Gouaux, Structural basis for recognition of diverse antidepressants by the human serotonin transporter. *Nat. Struct. Mol. Biol.* **25**, 170–175 (2018).

60. A. M. Abramyan *et al*., Computation-guided analysis of paroxetine binding to hSERT reveals functionally important structural elements and dynamics. *Neuropharmacology*, 10.1016/j.neuropharm.2018.10.040 (2018).
61. N. Eswar *et al*., Comparative protein structure modeling using MODELLER. *Curr. Protoc. Protein Sci.* **86**, 2.9.1–2.9.37 (2007).
62. W. Humphrey, A. Dalke, K. Schulten, VMD: Visual molecular dynamics. *J. Mol. Graph.* **14**, 33–38, 27–28 (1996).
63. J. Lee *et al*., CHARMM-GUI input generator for NAMD, GROMACS, AMBER, OpenMM, and CHARMM/OpenMM simulations using the CHARMM36 additive force field. *J. Chem. Theory Comput.* **12**, 405–413 (2016).
64. R. B. Best *et al*., Optimization of the additive CHARMM all-atom protein force field targeting improved sampling of the backbone φ, ψ and side-chain χ_1 and χ_2 dihedral angles. *J. Chem. Theory Comput.* **8**, 3257–3273 (2012).
65. J. B. Klauda *et al*., Update of the CHARMM all-atom additive force field for lipids: Validation on six lipid types. *J. Phys. Chem. B* **114**, 7830–7843 (2010).
66. U. Essmann *et al*., A smooth particle mesh Ewald method. *J. Chem. Phys.* **103**, 8577–8593 (1995).
67. J. C. Phillips *et al*., Scalable molecular dynamics with NAMD. *J. Comput. Chem.* **26**, 1781–1802 (2005).
68. D. E. Shaw *et al*., Anton, a special-purpose machine for molecular dynamics simulation. *Commun. ACM* **51**, 91–97 (2008).
69. R. A. Lippert *et al*., Accurate and efficient integration for molecular dynamics simulations at constant temperature and pressure. *J. Chem. Phys.* **139**, 164106 (2013).
70. W. G. Hoover, Canonical dynamics: Equilibrium phase-space distributions. *Phys. Rev. A Gen. Phys.* **31**, 1695–1697 (1985).
71. Schrödinger, Maestro (Version 2017-2, Schrödinger, LLC, New York, 2012).
72. A. D. Becke, Density-functional thermochemistry. III. The role of exact exchange. *J. Chem. Phys.* **98**, 5648–5652 (1993).
73. P. J. Stephens, F. J. Devlin, C. F. Chabalowski, M. J. Frisch, Ab initio calculation of vibrational absorption and circular dichroism spectra using density functional force fields. *J. Phys. Chem.* **98**, 11623–11627 (1994).
74. J. D. Chodera, A simple method for automated equilibration detection in molecular simulations. *J. Chem. Theory Comput.* **12**, 1799–1805 (2016).
75. R Development Core Team, R: A Language and Environment for Statistical Computing (R Foundation for Statistical Computing, 2011), vol. **1.**
76. S. Lata, A. Reichel, R. Brock, R. Tampé, J. Piehler, High-affinity adaptors for switchable recognition of histidine-tagged proteins. *J. Am. Chem. Soc.* **127**, 10205–10215 (2005).
77. F. Qin, Restoration of single-channel currents using the segmental k-means method based on hidden Markov modeling. *Biophys. J.* **86**, 1488–1501 (2004).
78. M. Quick, J. A. Javitch, Monitoring the function of membrane transport proteins in detergent-solubilized form. *Proc. Natl. Acad. Sci. U.S.A.* **104**, 3603–3608 (2007).
79. W. Schaffner, C. Weissmann, A rapid, sensitive, and specific method for the determination of protein in dilute solution. *Anal. Biochem.* **56**, 502–514 (1973).